Chinese Chemical Letters 35 (2024) 110355

Contents lists available at ScienceDirect

Chinese Chemical Letters

journal homepage: www.elsevier.com/locate/cclet

A TOC- and deposition-free electrochromic window driven by redox flow battery

Jinlong Li[a,1], Ruixin Li[a,1], Jiahui Liu[a,1], Ji-Quan Liu[a,b,*], Jia Xu[a], Xianglin Zhou[a], Yefan Zhang[a], Kairui Wang[a], Lin Lei[a], Gang Xie[a,b], Fengmei Wang[c], Ying Yang[a,b,*], Liping Cao[a,*]

[a] *Shaanxi Provincial Key Laboratory of Electroanalytical Chemistry, Shaanxi Provincial Key Laboratory of Modern Separation Science, Key Laboratory of Synthetic and Natural Functional Molecule of the Ministry of Education, College of Chemistry & Materials Science, Northwest University, Xi'an 710127, China*
[b] *Shaanxi Key Laboratory for Carbon Neutral Technology, Carbon Neutrality College (Yulin), Northwest University, Xi'an 710069, China*
[c] *State Key Laboratory of Chemical Resource Engineering, College of Chemistry, Beijing University of Chemical Technology, Beijing 100029, China*

ARTICLE INFO

Article history:
Received 12 July 2024
Revised 13 August 2024
Accepted 21 August 2024
Available online 23 August 2024

Keywords:
Electrochromic window
Redox flow battery
Free of TOC- and deposition layers
Iron complex
Indoor temperature modulation

ABSTRACT

Under “green architecture” principles, electrochromic smart windows are employed to adjust optical transmittance and indoor temperature, yet their high costs limit the wide application. Here, an electrochromic window is driven by a redox flow battery (RFB), where TOC and deposition layers are no longer needed. The transmittance of the electrochromic window is modulated by the state of oxidation (SOC) of aqueous posolyte $Fe(phen)_3Cl_2$, which is coupled with BTMAP-Vi negolyte in RFB. Under optimized conditions, average CE, VE, and EE reach 93.25%, 92.61%, and 86.35% for RFB with a capacity fading rate of 1.57% per cycle. 88.66% optical modulation and 9.36 cm^2/C coloration efficiency are achieved in the electrochromic process, and 72.34% optical modulation is maintained after 12000 s. Essentially, the indoor temperature declines 3 °C for posolyte with 100% SOC when compared with the control experiment using circulating water for a model house. This means minimum electricity of 0.0185 kWh is saved when using an air conditioner to cool a 100 m^3 house, which corresponds to declined CO_2 emission (COE) of 0.0185 kg. This work provides a novel and cost-efficient strategy for modulating indoor comfort *via* electrochromic windows driven by RFB.

Building energy consumption covers 30%~40% of global total energy consumption, *ca.* 1/3 of which is used for maintaining indoor comfort, such as heating, ventilation, and air-conditioning (HVAC) [1–3]. Of such huge energy consumption, *ca.* 45% is related to windows (*e.g.*, natural daylighting and solar heat) [4–6]. Static controls (*e.g.*, blinds or shades) are driven by mechanical force, however, they inevitably meet inconvenience in transportation, storage, and installation. Compared to these, the electrochromic smart windows can modulate optical transmittance dynamically *via* reversible electrochromic reactions [7–10], aligning with “green architecture” principles. Generally, electrochromic devices possess a sandwich structure containing transparent substrates, ion storage conductive layers, electrochromic conductive layers, and electrolyte layer (Scheme 1) [10–12]. The brief production process, period, and price of electrochromic glass are provided in Fig. S1 (Supporting information). Of course, manufacturing costs and process simplification for large-area electrochromic windows are challenging issues for wide applications [13,14]. The concept of TOC-free electrochromic windows has been developed by Wang *et al.* [15,16], based on redox-flow systems. In these works, electrochromic materials are employed in fabricating the coating layer, such as Prussian blue and TiO_2.

The present work employs an electrochromic electrolyte to tune light transmission in the smart window. It merits the advantage of avoiding the deposition process for fabricating the electrochromic layer. In this case, a seven-layered sandwich can be replaced by a three-layered one, reaching the goal of cost-effectiveness (Scheme 1). The abundance of electrochromic electrolytes in RFB provides a vast range of selection and possibilities [17–19]. A wide range of color control can be achieved to meet different application scenarios *via* adjusting applied current and voltage, as well as electrolyte concentration and composition. In contrast to traditional electrochromic layers, this electrochromic electrolyte can be regen-

---

[*] Corresponding authors.
E-mail addresses: jiquan-liu@nwu.edu.cn (J.-Q. Liu), yingyang@nwu.edu.cn (Y. Yang), chcaoliping@nwu.edu.cn (L. Cao).
[1] These authors contributed equally to this work.

https://doi.org/10.1016/j.cclet.2024.110355

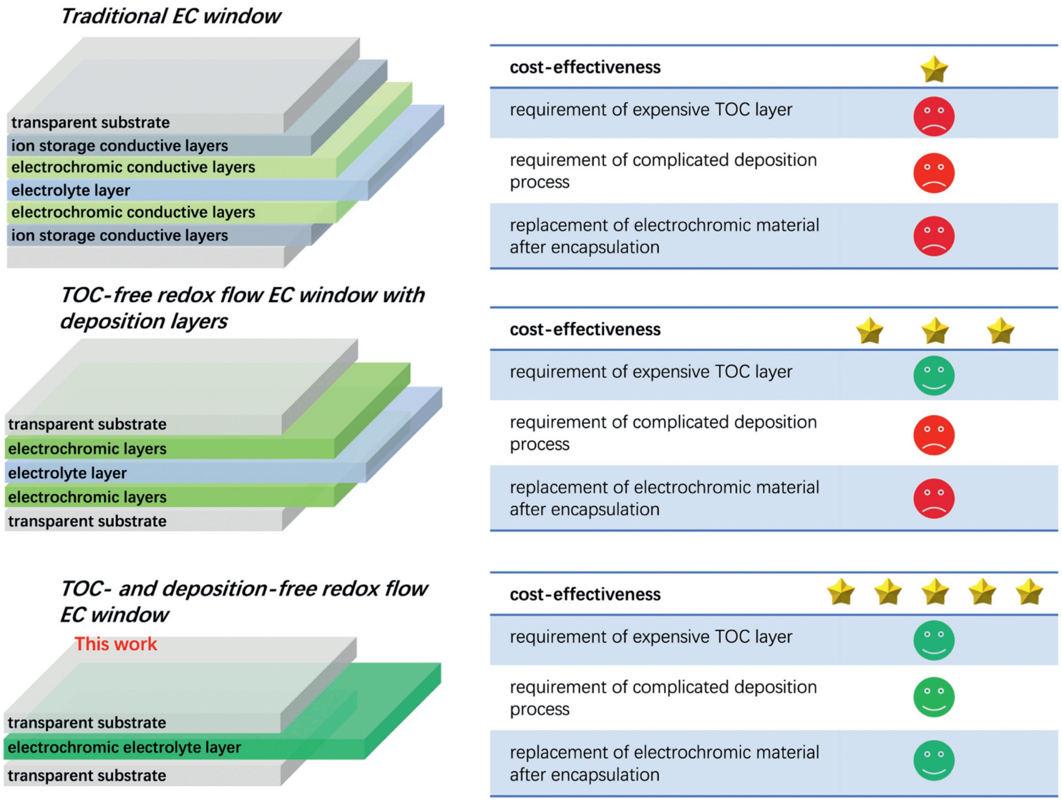

Scheme 1. Representation and comparison of electrochromic windows as well as the advantages of present work.

erated by updating the electrolyte in the storage tank. As a proof of concept, a phenanthroline-based metal complex ($Fe(phen)_3Cl_2$) is employed as the electrochromic electrolyte, and the transmittance of the electrochromic window is modulated by an RFB system.

In RFB, considerable progress has been achieved in developing posolytes containing iron (Fe) and its complexes, which merit the advantages of low cost and environmental friendliness [20–22]. Inspired by this, $Fe(phen)_3Cl_2$ is synthesized by a reaction between phenanthroline and $FeCl_2{\cdot}4H_2O$ in acetonitrile under reflux conditions (Fig. 1a). Red solid is obtained after column chromatography. Its chemical shifts (δ 8.80, 8.40, and 7.73 ppm) in ^1H NMR spectrum (Fig. S2 in Supporting information) and m/z 298.0635 in the high-resolution mass spectrum (Fig. S3 in Supporting information) confirm the success of synthesis. The molecular coordination is characterized by single-crystal X-ray diffraction, and its crystallographic data is listed in Table S1 (Supporting information), together with details of data collection and refinement. Similar to the literature [23], $Fe(phen)_3Cl_2$ crystallizes in the triclinic crystal structure, and its ORTEP diagram is shown in Fig. 1a and Fig. S1. In this distorted octahedral coordination, the average Fe—N bond length, N—Fe—N bite angle, and *trans* angle for opposite N atoms are 1.976~1.973 Å, 82.83°~83.06°, and 174.8°~175.93° (Tables S2 and S3 in Supporting information), respectively.

In RFB (Fig. 1b), $Fe(phen)_3Cl_2$ acts as a posolyte compound. Commercially available BTMAP-Vi is employed as a negolyte when considering its robust nature [24]. As illustrated by cyclic voltammetry (CV, Fig. 1c and Fig. S5 in Supporting information), the redox reaction for posolyte compound $Fe(phen)_3Cl_2$ involves one electron transfer with redox potential ($E_{1/2}$) of 0.836 V *vs.* SCE, while BTMAP-Vi serves as negolyte active molecule with $E_{1/2} = -0.592$ V *vs.* SCE for first electron redox reaction. Both exhibit good reversibility (Fig. S6 in Supporting information). In detail, the anodic peak current density decreases by 15% after 100 cycles when compared with the second cycle for $Fe(phen)_3Cl_2$, while the cathodic one increases by 5%. For BTMAP-Vi, its current densities incline by 9.7% for the anodic peak but decline by 14.4% for the cathodic peak. The kinetics of redox couples are evaluated *via* CV at various scan rates (Fig. S7 in Supporting information). Based on the Randles-Sevcik equation, diffusion coefficients for oxidized state (D^O) and reduced state (D^R) of $[Fe(phen)_3]^{3+}/[Fe(phen)_3]^{2+}$ are determined to be 2.743×10^{-6} and 1.457×10^{-6} cm^2/s (Fig. 1d), respectively. They are in the same range of reported ferric complexes ($2.3{\sim}2.8 \times 10^{-6}$ cm^2/s) [21,25,26]. In the same way, the first redox state $D_1{}^O$ and $D_1{}^R$ of $[BTMAP\text{-}Vi]^{3+}$ and $[BTMAP\text{-}Vi]^{4+}$ are measured to be 4.836×10^{-6} and 2.736×10^{-6} cm^2/s, respectively, comparable to reported ones [27].

The performance of RFB is optimized and evaluated under various conditions. Initially, the impact of ion exchange membrane is investigated, and the Nafion 117 cation membrane is selected to separate posolyte and negolyte (Table S4, Figs. S8 and S9 in Supporting information). As illustrated in Fig. 1e, the RFB delivers a working voltage of 1.428 V. Its open circuit voltage (OCV) increases from 1.386 V at 10% SOC to 1.475 V at 50% SOC, and further to 1.581 V at 90% SOC. Across all SOC ranges, the high-frequency area-specific resistance (ASR) of the battery is measured to be 4.9 Ω/cm, which comes from membrane resistance and is also affected by the presence of acetonitrile residue (Fig. S10 in Supporting information). The polarization resistance varies in the range of 6.56~6.61 Ω/cm. Namely, *ca.* 88% of total resistance derives from constant membrane resistance, while the rest 12% is due to kinetic losses in reducing ferric complex and its dimerization [21].

Galvanostatic charging and discharging (GCD) curves are displayed in Figs. S11a–c (Supporting information), at the applied current density of 3~5 mA/cm^2. Two discernable discharge plateaus are obtained at 1.5~1.1 V and 0.3~0 V, respectively. The presence of ferric dimer $[Fe_2O(phen)_4Cl_2]^{2+}$ with low redox potential accounts for the presence of a second discharge plateau (Scheme S1 in Supporting information) [21,22]. It derives from

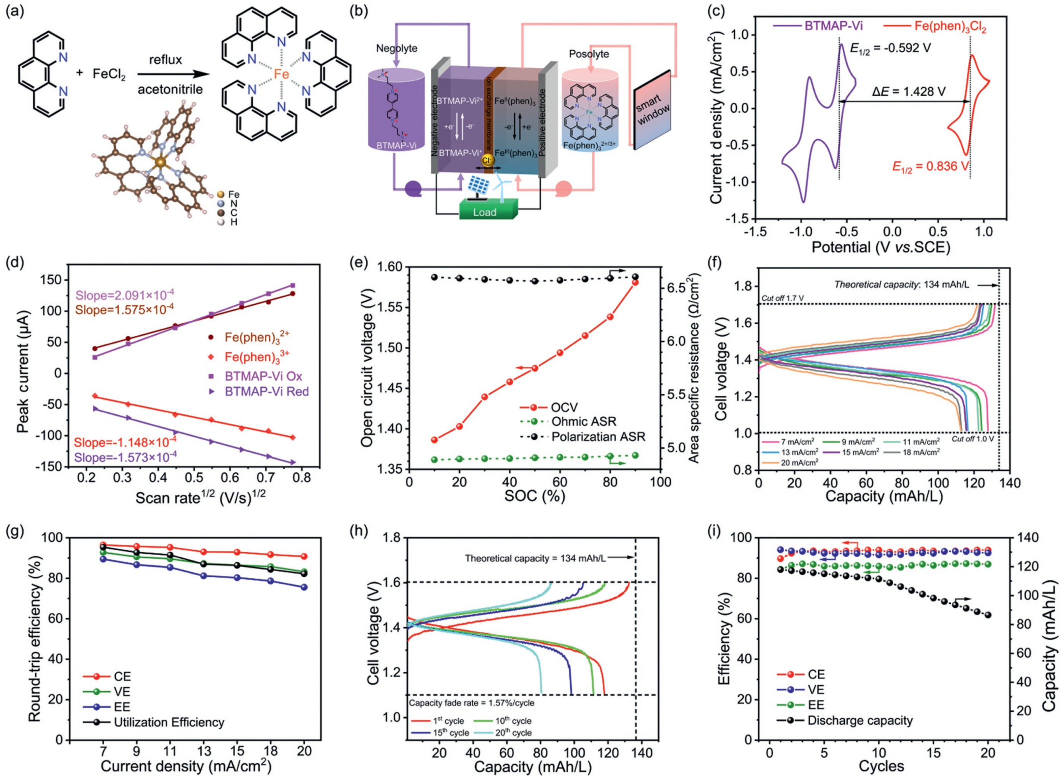

Fig. 1. (a) Synthesis and ORTEP diagram of Fe(phen)$_3$Cl$_2$. (b) Schematic drawing of RFB. (c) CV and (d) diffusion coefficients of Fe(phen)$_3$Cl$_2$ posolyte and BTMAP-Vi negolyte. (e) Plots of OCV, high frequency, and polarization ASR at various SOCs of RFB. (f, g) GCD curves and corresponding round-trip CE, VE, EE and utilization efficiency at different current densities. (h, i) Stability performance under current density of 7 mA/cm^2.

the dimerization of Fe(phen)$_3$Cl$_2$ with releasing of protonated ligand (H(phen)$^+$). More dimers are generated at lower current density, owing to extended discharging reaction time. Nevertheless, this trivially affects the volume capacity, since the reverse reaction could happen between [Fe$_2$O(phen)$_4$Cl$_2$]$^{2+}$ and H(phen)$^+$, and affords [Fe(phen)$_3$]$^{2+}$ [21,22]. A trade-off effect is obtained between Coulombic efficiency (CE) and voltage efficiency (VE) at different discharge voltage cut-offs (Fig. S12 in Supporting information). Under the current density of 5 mA/cm^2, CE reaches 63% at relatively low VE (88%) at 1.0 V discharge voltage cut-off, whilst 98% CE and 46% VE are obtained at 0.001 V discharge voltage cut-off. The incomplete release of storage energy (utilization of capacity) at high voltage cut-off accounts for relatively poor CE. Under large current density, the first discharge plateau extended at the expense of the second discharge plateau (Figs. S11d–i in Supporting information). This means large current density is beneficial to battery performance. To avoid dimmer formation during the discharge process, the discharge voltage cut-off is set to be 1.0 V, and battery performance is further evaluated at different current densities (7∼20 mA/cm^2) for the first discharge plateau (Fig. 1f). When increasing the current density, the charge plateau ascends, accompanied by a descent of the discharge plateau. The declined capacity utilization efficiency is attributed to increased ohmic resistance at large current density, as well as overpotential related to mass transport (polarization). Under optimized current density (7 mA/cm^2), the charge and discharge volume capacities are 131.73 and 127.70 mAh/L, which correspond to 98.31% and 95.36% of theoretic capacity. At the same time, the battery exhibits 96.45% CE, 92.75% VE, and 89.46% EE (Fig. 1g). The impact of electrolytes on the electrochemical performance and recyclability of Fe(phen)$_3$Cl$_2$ is investigated as well, and glycine-HCl buffer with a pH of 2.5 turns out to be the optimal electrolyte (Fig. S13 in Supporting information). Under optimized conditions (current density 7 mA/cm^2, glycine-HCl buffer, pH 2.5), the battery is charged and discharged between 1.8 V and 0.001 V (Fig. 1h). During 20 cycles, the average CE, VE, and EE reach 93.25%, 92.61%, and 86.35% (Fig. 1i and Fig. S14 in Supporting information). The volume capacity at the first cycle is 117.34 mAh/L (87.31% of theoretic value) and declines to 80.48 mAh/L (60.10% of theoretic value). The capacity fading rate is 1.57% per cycle, better than one without glycine-HCl butter (Figs. S8 and S9 in Supporting information). Self-discharge of [Fe$_2$O(phen)$_4$Cl$_2$]$^{2+}$ and its precipitation may lead to capacity decay (Scheme S1), together with the crossover of H(phen)$^+$ [21,22]. Another possibility is the decomposition of Fe(phen)$_3{}^{2+}$ and Fe(phen)$_3{}^{3+}$ in aqueous electrolyte (Scheme S2 in Supporting information), which, however, can be efficiently retarded by introducing glycine-HCl buffer.

The absorption spectra of [Fe(phen)$_3$]$^{3+}$/[Fe(phen)$_3$]$^{2+}$ in the UV–vis region are recorded at various SOCs (Fig. 2a). At SOC of 0%, the absorption maximum wavelength (λ_{max}) of the posolyte appears at 510 nm (Fig. S15 in Supporting information). This is ascribed to the excitation of [Fe(phen)$_3$]$^{2+}$ from low spin singlet state ($^1A_1$) to metal-to-ligand charge transfer state (^{1}MLCT) [28,29]. Its aqueous solution is featured in an orange-red color. After oxidation, λ_{max} shifts to 610 nm for [Fe(phen)$_3$]$^{3+}$ (or Fe(III) complexes, Fig. S16 in Supporting information) [30]. This absorption derives from $\pi \rightarrow t_{2g}$ ligand-to-metal charge transfer (LMCT) over Fe(phen)$^{3+}$ [31]. During the galvanostatic charging process (Fig. 2b), the posolyte SOC increases and its color trajectory is depicted in the International Commission on Illumination (CIE) 1931 color space (Fig. 2c). In this curved segment (ABCDEFG), the red-to-blue ratios (x) decline from 0.59 to 0.23, and the green-to-blue ratios (y) decrease from 0.37 (A) to 0.26 (G). In the discharging process, however, its color trajectory (GF'E'D'C'BA) does not coincide with the A-to-G curve. The main difference relies on x values. Taking 30% SOC for instance ($y = 0.36$), its x values are equal to 0.42 and 0.48 in

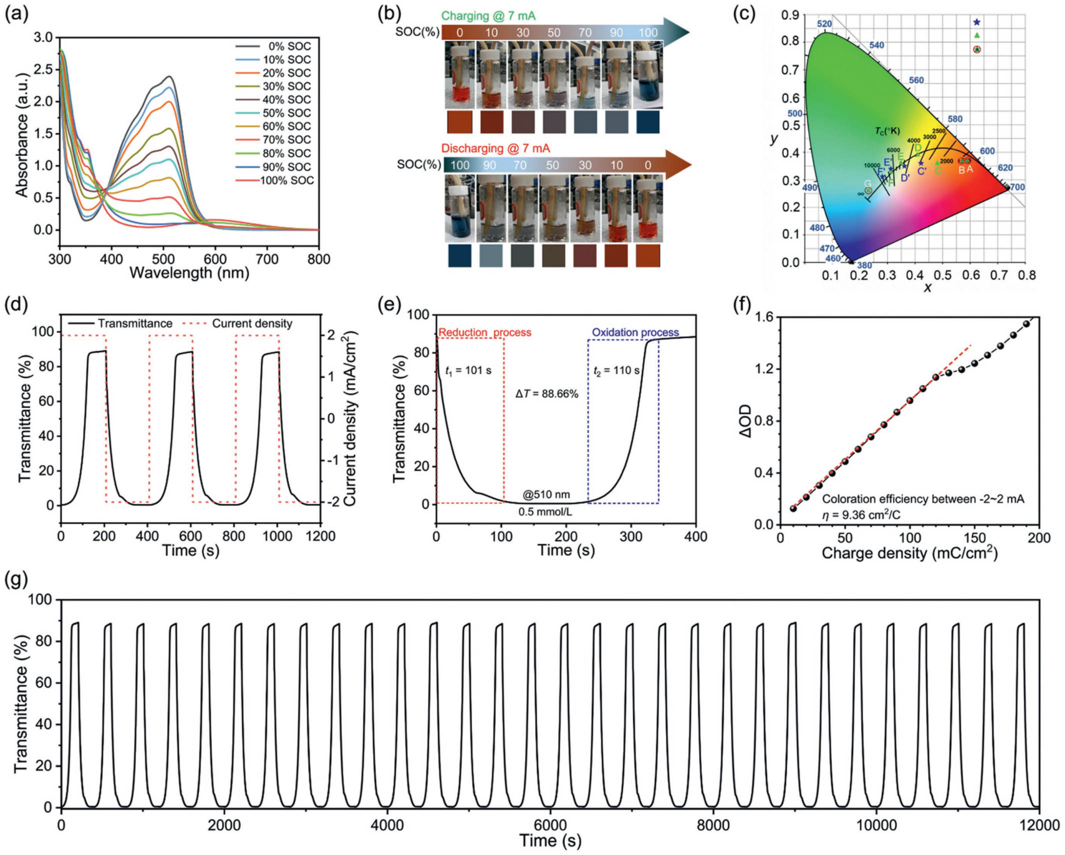

Fig. 2. (a, b) Absorbance changes and color change of posolyte at different SOC. (c) CIE chromaticity coordinates charts and color trajectory. (d, e) Transmittance response curves. (f) Coloration efficiency. (g) Transmittance stability curve in long-term GCD test.

charging and discharging processes, respectively. For $[Fe(phen)_3]^{3+}$ and $[Fe(phen)_3]^{2+}$, their stability constants ($\lg K_{stab}$) are 14.1 and 21.3 [31–34], respectively. Compared to the reduced state, relatively low stability constant and irreversible degradation of $[Fe(phen)_3]^{3+}$ at high oxidation state might account for the observed inconformity in color trajectories.

The optical modulation (ΔT) is defined as the transmittance difference of bleached ($T_b(\lambda)$) and colored state ($T_c(\lambda)$). At $\lambda = 510$ nm, ΔT of posolyte firstly increases along the concentration and reaches a maximum of 88.66% (0.5 mol/L), and thereafter declines drastically. Then, the electrochromic behaviors of the posolyte are characterized *via in-situ* recording of transient transmittance at $\lambda = 510$ nm. Under chronoamperometry, the continuous switches between colored (100% SOC) and decolored states (0% SOC) are carried out at current density of 2 mA/cm^2 for 200 s each (Fig. 2d). In accordance, the response time is estimated to be 101 s in the reduction process and increases to 110 s in the oxidation process (Fig. 2e). Namely, the coloration/decoloration switching can be achieved within 2 min, slightly shorter than the redox system between redox shuttle anthraquinone-2,6-disulfonate (AQDS) and targeting material $K_3Fe_4[Fe(CN)_6)]_3$ [15]. The obtained response time is lower than the theoretic value (120.5 s), relating to incomplete capacity utilization during the redox reactions. The difference in response time in reduction and oxidation processes is again correlated to low $\log K_{stab}$ and irreversible degradation of $[Fe(phen)_3]^{3+}$. The energy consumption in the electrochromic process is evaluated *via* coloration efficiency (η) based on its definition Eq. 1 [35]. Here, ΔOD is the variation of optical density, defined as $\lg(T_b/T_c)$. Q and A represent the consumed charge and electrode surface area. At $\lambda = 510$ nm, $\eta = 9.36$ C^{-1} is obtained for posolyte (Fig. 2f). Compared to solid (or condensed) electrochromic material, large electrolyte volume in the electrochromic window and RFB system mainly accounts for its low η value. At a given concentration (c), Q increases linearly with electrolyte volume (V) according to Faraday's law $Q = zFcV$ ($z = 1$). In the presence system, η would be 46 cm^2/C when V reduces to 1 mL. The recycling stability is investigated as well (Fig. 2g). This system can work stably over 12000s. After 25 cycles, ΔT declines to 72.34%, which is related to the partial degradation of $[Fe(phen)_3]^{3+}$.

$$\eta = \frac{\Delta \mathrm{OD}}{\frac{Q}{A}} = \frac{\lg\left(\frac{T_b}{T_c}\right)}{\frac{Q}{A}} \tag{1}$$

In real practice, an electrochromic window (4.5 cm × 5.5 cm × 1.0 cm) is equipped/installed on a model house (Fig. 3a, Figs. S17 and S18 in Supporting information) to tune the transmittance of simulated sunlight (300 W Xe lamp). The indoor temperature is monitored by a thermometer. In the absence of electrolyte (blank), the temperature increases drastically from 22.0 °C to 31.2 °C within 35 min and reaches 32.6 °C after 180 min (Fig. 3b). Under the same irradiation, different temperature trends are obtained in the presence of posolyte. Under various SOC states, the sequence of maximum temperature is 100% SOC < 10% SOC < 0% SOC < 30% SOC < 90% SOC < 50% SOC < 70% SOC. For posolyte at 100% SOC, the indoor temperature surges to 27.3 °C after 45 min irradiation and inclines smoothly to its maximum (29.3 °C) thereafter. Considering the absorbed solar energy mainly emits to the surroundings (indoor air and posolyte), water is employed in the control experiment. Its temperature profile is similar to the blank one, where the maximum indoor temperature reaches 32.2 °C. This means posolyte itself mainly contributes to declined temperature under irradiation. Referring to water control, the declined indoor temperature (ΔT_{indoor}) is calculated *via* Eq. 2.

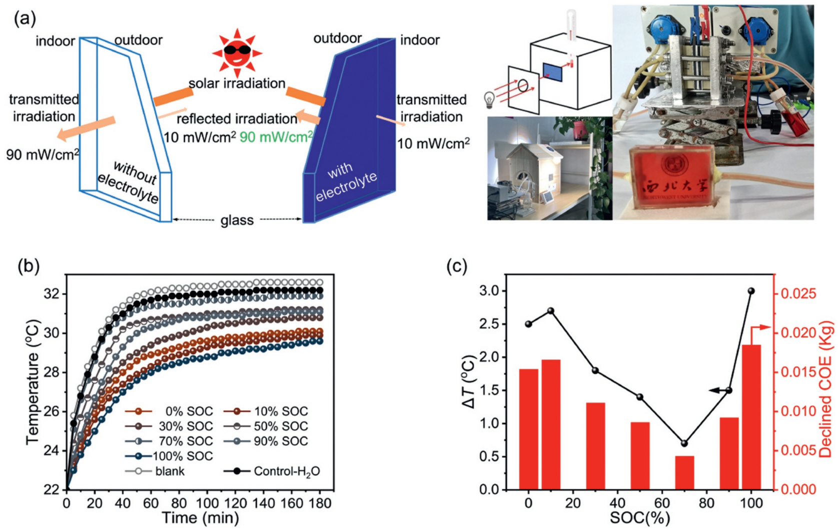

Fig. 3. (a) Schematic drawing and photographs of the electrochromic window, RFB system, and as-prepared house model. (b) Indoor temperature variations along irradiation time at different SOCs. (c) Declined indoor temperature and COE when referring to water.

With redox-flow electrochromic window, the saved energy can be reflected by heat difference (ΔQ_{indoor}), which can be calculated by Eq. 3 for a house (indoor space $V = 100\ m^3$) with identical glazing ratio to the model house (window-wall ratio of 0.0274). The specific heat capacity (c) and density (ρ) of air are 10^3 J/kg and 1.29 kg/m^3, respectively.

$$\Delta T_{indoor} = T_{indoor}(water) - T_{indoor}(posolyte) \tag{2}$$

$$\Delta Q_{indoor} = c\rho V \Delta T_{indoor} \tag{3}$$

Assuming this indoor temperature difference ΔT_{indoor} is modulated by an air conditioner, the consumed electric energy (W_e) is estimated *via* Eq. 4 [36], where EER is the energy efficiency ratio of the air conditioner. The calculation details and obtained results are summarized in Fig. 3c and Tables S4 and S5 (Supporting information). The minimum W_e saved in a 100 m^3 house is 66.72 kJ (0.0185 kWh). Then, the COE amount is obtained according to Eq. 5, where 0.998 kg/kWh is the standard coal emission factor for 1 kWh of electricity [37]. At SOC of 100%, the reduced COE reaches a maximum (0.0185 kg). On the contrary, a posolyte with 70% SOC exhibits the lowest efficiency in modulating indoor temperature. The electricity consumed by pumps for circulating electrolytes in the double-layered window and RFB is estimated to be 3.38 and 1.13~1.69 Wh, respectively. To be noted, solar cells can be employed to drive the pump. This would make our electrochromic window and RFB system more sustainable in saving energy.

$$W_e = \frac{\Delta Q_{indoor}}{EER} \tag{4}$$

$$COE = W_e \times 0.998 \tag{5}$$

To sum up, triclinic crystalline Fe(phen)$_3$Cl$_2$ is employed as a posolyte in the electrochromic window and RFB system, and its redox stability is improved in the glycine-HCl buffer. Coupled by BTMAP-Vi negolyte, an OCV of 1.475 V at 50% SOC is achieved for RFB. The absorption difference of $[Fe(phen)_3]^{3+}/[Fe(phen)_3]^{2+}$ is utilized to modulate the transmittance of the model house and indoor temperature. Compared to circulating water, the indoor temperature decreased by 0.7~3 °C at various SOCs of posolyte. For maximum $\Delta T_{indoor} = 3$ °C, *ca.* 0.0185 kWh electric energy is saved in a 100 m^3 house, corresponding to declined COE of 0.0185 kg. It can be operated stably for over 12000s with 72.34% optical modulation preservation and a capacity fading rate of 1.57% per cycle. As a prototype of the electrochromic window, this work provides a cost-efficient strategy to reduce its cost, however, more works are still needed in developing electrochromic molecules with high stability and coloration efficiency concerning long-term operation and fast response.

Declaration of competing interest

The authors declare that they have no known competing financial interests or personal relationships that could have appeared to influence the work reported in this paper.

CRediT authorship contribution statement

Jinlong Li: Writing – original draft, Investigation, Data curation. **Ruixin Li:** Writing – original draft, Methodology, Investigation. **Jiahui Liu:** Investigation, Data curation. **Ji-Quan Liu:** Investigation, Data curation. **Jia Xu:** Investigation, Data curation. **Xianglin Zhou:** Investigation, Data curation. **Yefan Zhang:** Investigation, Data curation. **Kairui Wang:** Resources. **Lin Lei:** Resources, Methodology. **Gang Xie:** Resources. **Fengmei Wang:** Resources, Methodology, Conceptualization. **Ying Yang:** Writing – review & editing, Validation, Methodology, Funding acquisition, Conceptualization. **Liping Cao:** Writing – review & editing, Supervision.

Acknowledgments

The authors appreciate the financial supports from the National Natural Science Foundation of China (No. 22122108) and the Luohe Xinwang Chemical Co., Ltd., China. The "Top-rated Discipline" construction scheme of Shaanxi higher education in China supported part of this work.

Supplementary materials

Supplementary material associated with this article can be found, in the online version, at doi:10.1016/j.cclet.2024.110355.

References

[1] B. Richter, D. Goldston, G. Crabtree, et al., Rev. Mod. Phys. 80 (2008) S1–S109.
[2] X. Cao, X. Dai, J. Liu, Energy Build. 128 (2016) 198–213.
[3] D.M. Kammen, D.A. Sunter, Science 352 (2016) 922–928.
[4] A. Ghosh, R. Hafnaoui, A. Mesloub, et al., J. Build. Eng. 84 (2024) 108644.

[5] S. Grynning, A. Gustavsen, B. Time, B.P. Jelle, Energy Build. 61 (2013) 185–192.
[6] Q. Tushar, M.A. Bhuiyan, G. Zhang, J. Cleaner Produc. 330 (2022) 129936.
[7] C. Gu, A.B. Jia, Y.M. Zhang, S.X.A. Zhang, Chem. Rev. 122 (2022) 14679–14721.
[8] H. Gong, W. Li, G. Fu, et al., J. Mater. Chem. A 10 (2022) 6269–6290.
[9] H. Fu, L. Zhang, Y. Dong, C. Zhang, W. Li, Mat. Chem. Front. 7 (2023) 2337–2358.
[10] S. Wu, H. Sun, M. Duan, et al., Cell Rep. Phys. Sci. 4 (2023) 101370.
[11] V.K. Thakur, G. Ding, J. Ma, P.S. Lee, X. Lu, Adv. Mater. 24 (2012) 4071–4096.
[12] C.G. Granqvist, M.A. Arvizu, İ. Bayrak Pehlivan, et al., Electrochim. Acta 259 (2018) 1170–1182.
[13] Cost-benefit analysis of smart glass, https://www.smartglassworld.net/cost-benefit-smart-glass.
[14] C.M. Lampert, Sol. Energy Mater. Sol. Cells 76 (2003) 489–499.
[15] R. Yan, L. Liu, H. Zhao, et al., J. Mater. Chem. C 4 (2016) 8997–9002.
[16] J.R. Jennings, W.Y. Lim, S.M. Zakeeruddin, M. Grätzel, Q. Wang, ACS Appl. Mater. Interfaces 7 (2015) 2827–2832.
[17] Z. Zhao, X. Liu, M. Zhang, et al., Chem. Soc. Rev. 52 (2023) 6031–6074.
[18] Z. Li, Y.C. Lu, Adv. Mater. 32 (2020) 2002132.
[19] P. Poizot, J. Gaubicher, S. Renault, et al., Chem. Rev. 120 (2020) 6490–6557.
[20] Q. Xu, S. Wang, C. Xu, et al., Chin. Chem. Lett. 34 (2023) 108188.
[21] J. Gao, K. Amini, T.Y. George, et al., Adv. Energy Mater. 12 (2022) 2202444.
[22] W. Ruan, J. Mao, S. Yang, Q. Chen, J. Electrochem. Soc. 167 (2020) 100543.
[23] V.V. Avdeeva, A.V. Vologzhanina, L.V. Goeva, E.A. Malinina, N.T. Kuznetsov, Z. Anorg. Allg. Chem. 640 (2014) 2149–2160.
[24] S. Liu, M. Zhou, T. Ma, et al., Chin. Chem. Lett. 31 (2020) 1690–1693.
[25] M.T. Carter, M. Rodriguez, A.J. Bard, J. Am. Chem. Soc. 111 (1989) 8901–8911.
[26] X. Li, P. Gao, Y.Y. Lai, et al., Nat. Energy 6 (2021) 873–881.
[27] X.L. Lv, P. Sullivan, H.C. Fu, et al., ACS Energy Lett. 7 (2022) 2428–2434.
[28] J. Tribollet, G. Galle, G. Jonusauskas, et al., Chem. Phys. Lett. 513 (2011) 42–47.
[29] B.C. Paulus, K.C. Nielsen, C.R. Tichnell, M.C. Carey, J.K. McCusker, J. Am. Chem. Soc. 143 (2021) 8086–8098.
[30] A.A.G.A. Al Mahdi, M.A. Hussein, C.C. Joubert, J.C. Swarts, C.R. Dennis, Polyhedron 81 (2014) 409–413.
[31] S. Sahami, R.A. Osteryoung, Inorg. Chem. 23 (1984) 2511–2518.
[32] M.A. Proskurnin, V.V. Chernysh, M.Y. Kononets, S.V. Pakhomova, Russ. Chem. Bull. 54 (2005) 124–134.
[33] B. Zhang, S. Liu, Y. Zhu, et al., Univ. Chem. 37 (2022) 2110066.
[34] T.S. Lee, I.M. Kolthoff, D.L. Leussing, J. Am. Chem. Soc. 70 (1948) 2348–2352.
[35] H. Sun, W. Wang, Y. Xiong, et al., Chin. Chem. Lett. 35 (2024) 109213.
[36] M.F.H. Rani, Z.M. Razlan, A.B. Shahriman, et al., IOP Conf. Ser.: Mater. Sci. Eng. 429 (2018) 012070.
[37] B. Cheng, Z. Chen, B. Yu, et al., IEEE J. Sel. Top. Appl. Earth Observ. Remote Sens. 13 (2020) 675–684.